2010

Inverse Martensitic Transformation in Zr Nanowires

Suzhi Li
Xi'an Jiaotong University

Xiangdong Ding
Xi'an Jiaotong University

Ju Li
University of Pennsylvania, liju@seas.upenn.edu

Xiaobing Ren
Xi'an Jiaotong University

Jun Sun
Xi'an Jiaotong University

See next page for additional authors

Suggested Citation:
Li, S. Z, Ding, J. Li, X. Ren, et. al. "Inverse martensitic transfromation in Zr nanowires." *Physical Review B* Vol. 81, 245433.

http://dx.doi.org/10.1103/PhysRevB.81.245433

Inverse Martensitic Transformation in Zr Nanowires

Abstract
Like martensitic transformations (MTs), inverse martensitic transformations (IMTs) are shear-dominant diffusionless transformations, but are driven by reduction in interfacial energies rather than bulk free energies, and exhibit distinctive behavior such as instantaneous initiation (like spinodal decomposition) and self-limiting lengthscale. Bulk Zr metal is known to undergo normal MT from the high-temperature bcc phase to the low-temperature hcp phase. Using molecular dynamics simulations we demonstrate that, unlike in the bulk, an IMT to the bcc structure can occur in (1100)-oriented hcp Zr nanowires at low temperatures, which is driven by the reduction in the nanowire surface energy. The bcc domains subsequently become distorted and transform into a new (1120)-oriented hcp domain, leading to reorientation of the nanowire. This behavior has implications for the study of structural transformations at the nanoscale and surface patterning.

Disciplines
Engineering | Materials Science and Engineering

Comments
Suggested Citation:
Li, S. Z, Ding, J. Li, X. Ren, et. al. "Inverse martensitic transfromation in Zr nanowires." *Physical Review B* Vol. 81, 245433.

http://dx.doi.org/10.1103/PhysRevB.81.245433

Author(s)
Suzhi Li, Xiangdong Ding, Ju Li, Xiaobing Ren, Jun Sun, Evan Ma, and Turab Lookman

Inverse martensitic transformation in Zr nanowires

Suzhi Li,[1] Xiangdong Ding,[1,2,*,†] Ju Li,[1,3,*,‡] Xiaobing Ren,[1,4] Jun Sun,[1] Evan Ma,[1,5,*,§] and Turab Lookman[2]
[1]*State Key Laboratory for Mechanical Behavior of Materials, Xi'an Jiaotong University, Xi'an 710049, China*
[2]*Theoretical Division, Los Alamos National Laboratory, Los Alamos, New Mexico 87545, USA*
[3]*Department of Materials Science and Engineering, University of Pennsylvania, Philadelphia, Pennsylvania 19104, USA*
[4]*Ferroic Physics Group, National Institute for Materials Science, Tsukuba, 305-0047 Ibaraki, Japan*
[5]*Department of Materials Science and Engineering, Johns Hopkins University, Baltimore, Maryland 21218, USA*
(Received 24 January 2010; revised manuscript received 4 May 2010; published 28 June 2010)

Like martensitic transformations (MTs), inverse martensitic transformations (IMTs) are shear-dominant diffusionless transformations, but are driven by reduction in interfacial energies rather than bulk free energies, and exhibit distinctive behavior such as instantaneous initiation (like spinodal decomposition) and self-limiting lengthscale. Bulk Zr metal is known to undergo normal MT from the high-temperature bcc phase to the low-temperature hcp phase. Using molecular dynamics simulations we demonstrate that, unlike in the bulk, an IMT to the bcc structure can occur in $\langle \bar{1}100 \rangle$-oriented hcp Zr nanowires at low temperatures, which is driven by the reduction in the nanowire surface energy. The bcc domains subsequently become distorted and transform into a new $\langle \bar{1}\bar{1}20 \rangle$-oriented hcp domain, leading to reorientation of the nanowire. This behavior has implications for the study of structural transformations at the nanoscale and surface patterning.

DOI: 10.1103/PhysRevB.81.245433 PACS number(s): 64.70.Nd, 64.60.Bd, 62.23.Hj

I. INTRODUCTION

Martensitic transformation (MT) is a well-known diffusionless transition that occurs in materials undergoing solid-to-solid phase changes.[1–4] On the basis of Zener's model,[3] the parent phase is stable at high temperatures and usually has a relatively open structure which transforms into the (often more close packed) product phase upon cooling below a martensite-start temperature. Pure Zr, for example, undergoes such a MT from the high-temperature bcc structure to the low-temperature hcp phase, which is the most stable bulk phase at 0 K. This transition has been well studied in the bulk and follows the mechanism originally proposed by Burgers.[5]

In classic MT nucleation [Fig. 1(a)],[6] the bulk energy $V\Delta g_{\text{bulk}}<0$ is the driving force (proportional to the transformed volume V), whereas the interfacial energy $A\Delta\bar{\gamma}>0$ (proportional to the area A of the transformed region, where $\bar{\gamma}\equiv\frac{\Sigma_i\gamma_i A_i}{\Sigma_i A_i}$ is averaged over all interfaces that may include surfaces, where V, A_i are the pre-transformed volume and areas, respectively, even for post-transformed configuration, i.e., Lagrangian measure of $\Delta g_{\text{bulk}}, \bar{\gamma}$) works against the bulk driving force, from which one can derive a positive saddle energy. This means that for any finite driving force $\Delta g_{\text{bulk}}<0$, there is a positive activation barrier energy and waiting time for the nucleation of martensite, according to the reaction rate theory for the formation of the critical nucleus.[7] Once the activation barrier is overcome, the system transforms in a downhill process, with no bounds on the transformation V.

In inverse martensitic transformations (IMTs), the interfacial energy becomes the driving force and the bulk energy now works *against* the transformation, as shown in Fig. 1(b). Here $A\Delta\bar{\gamma}<0$, $V\Delta g_{\text{bulk}}>0$; both are inverted from those of normal MT, hence the name IMT. Two consequences can be seen from Fig. 1(b): (a) there is no nucleation barrier for IMT, i.e., IMT can happen instantaneously the moment $\Delta\bar{\gamma}$ turns negative and (b) IMT will stop automatically at a certain length scale $r^*\propto\Delta\bar{\gamma}/\Delta g_{\text{bulk}}$, as the rising bulk energy prevents further transformation. Thus, unlike isothermal MT which waits for a while (and therefore requires finite undercooling to be observable at laboratory time scale) but then keeps going once the barrier is overcome, IMT should happen nearly instantaneously but self stops at r^*.

Similar energetics as Fig. 1(b) is found in surface premelting phenomena, and is the reason that the melting of simple metals typically requires no superheating, whereas their solidifications require finite undercooling, as indicated by the time-temperature-transformation diagrams.[7] The difference is that surface premelting is a diffusive process whereas IMT is diffusionless. Therefore, IMT should be observable at low temperatures as diffusion is not required. In a semi-infinite half-space (height $H=\infty$) with open surface, the elasticity aspect of IMT and the finite length scale r^* may be utilized to introduce nanoscale patterning of the surface. If the sample

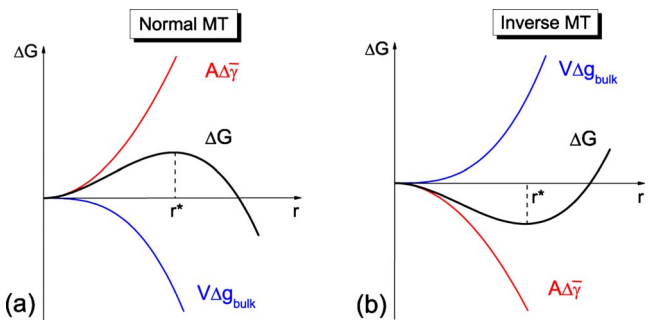

FIG. 1. (Color online) A comparison of the free energy landscape for (a) the normal MT and (b) the IMT, where r^* is characteristic size of the transformed region. In (a), the driving force is the bulk free energy $V\Delta g_{\text{bulk}}<0$ and the interfacial energy $A\Delta\bar{\gamma}>0$ opposes the transformation. In (b), the interfacial energy $A\Delta\bar{\gamma}<0$ provides the driving force whereas the bulk free energy $V\Delta g_{\text{bulk}}>0$ opposes it.

length scale H is comparable or smaller than r^*, however, IMT can be expected to finish throughout the sample (see our simulation below).

In this paper, we demonstrate such IMT at room temperature (RT), on the surface of Zr nanowires (NWs). In contrast to the normal MT where bcc transforms to hcp, a hcp to bcc transition is found instead, driven by the minimization of the surface energy of the NW, which becomes controlling for systems with very large surface-to-volume ratio. The surface energy minimization is accomplished via a two-step process: the initial $\langle\bar{1}100\rangle$-oriented Zr nanowire first undergoes IMT to the bcc configuration and becomes distorted, and subsequently undergoes a normal MT to a new $\langle\bar{1}\bar{1}20\rangle$-oriented hcp configuration. Similar surface-driven structural changes, such as crystal reorientation via twinning, have been revealed by molecular dynamics (MD) simulations in fcc (Au, Cu) (Refs. 8–10) and bcc (W) (Ref. 11) metallic NWs.

II. METHODS

We have used embedded atom method potentials for Zr (Refs. 12 and 13) to perform the MD simulations. These potentials reproduce very well the properties such as the cohesive energy, elastic constants, and especially the MT between bcc and hcp. In the following, we show the results obtained using the Zr potential developed by Mendelev and Ackland.[13] We first created the hcp $\langle\bar{1}100\rangle$-oriented nanowire with orientations of x-$[\bar{1}100]$, y-$[\bar{1}\bar{1}20]$, and z-$[0001]$ at 0 K. The cross section of the nanowire (y and z axes) is close to square with the [0001] side length in the range of 1.0–2.6 nm. The initial length of nanowire (x axis) is a factor of ten larger than the length of the cross section. The wire is then heated to 300 K at the rate of 100 K/ps and then relaxed at 300 K for 50 ps using the Nosé-Hoover thermostat.[14,15] During the above process, free boundary condition in three dimensions is used. The MD calculation is carried out using the LAMMPS code[16] with the atomic configurations displayed using ATOMEYE.[17]

III. RESULTS AND DISCUSSION

When the $\langle\bar{1}100\rangle$-oriented Zr NW is relaxed at 300 K for several picoseconds, the initial hcp configuration spontaneously undergoes IMT to transform to the bcc structure (x-$[10\bar{1}]$, y-[010], and z-[101]). As seen in Figs. 2(a) and 2(b), the bcc phase initiates on $\{\bar{1}\bar{1}20\}$ surface planes in the middle section of the wire and then spreads toward the ends and the interior. With the bcc formation, the phase boundaries divide the wire into three phase domains, one with the bcc structure at the center of the NW and the others with hcp structure at the ends. However, the phase boundaries do not move across the whole wire to convert the entire wire into the bcc phase, which undergoes severe compressive deformations along the wire axis to a new bcc configuration (x-[010], y-$[10\bar{1}]$, and z-[101]), as shown in Fig. 2(c). Finally, the distorted bcc phase gives way to a new $<\bar{1}\bar{1}20>$-oriented hcp configuration (x-$[\bar{1}\bar{1}20]$, y-$[\bar{1}100]$, and z-[0001]) in a normal bcc-to-hcp MT [Fig. 2(d)]. Compared to the initial $\langle\bar{1}100\rangle$ wire, the $\langle\bar{1}\bar{1}20\rangle$-oriented hcp unit cell can be considered to have rotated 30°, and this crystal reorientation is not completed directly by twinning as in fcc (Refs. 8–10) and bcc nanowires[11] but via the two-step IMT-MT processes shown above.

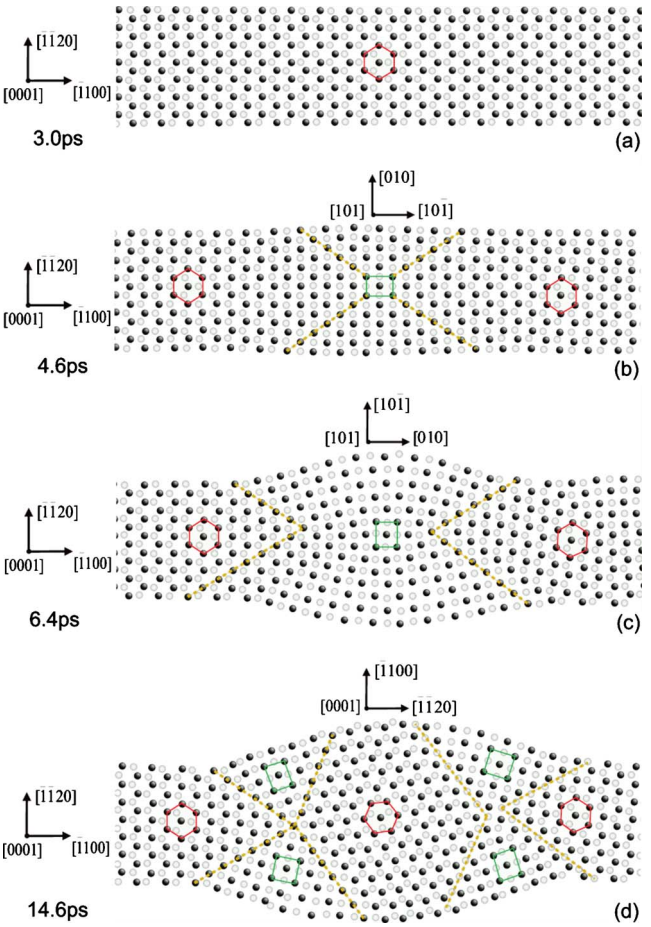

FIG. 2. (Color online) The two-step phase transition in a hcp Zr nanowire (21.2 nm × 2.1 nm × 2.1 nm) at 300 K. (a) Initially created hcp configuration with axis along $[\bar{1}100]$. (b) The hcp configuration transforms to the bcc configuration in the middle section of the wire with axis along $[10\bar{1}]$. (c) The transformed bcc phase is further distorted to a new [010]-axis configuration which shrinks in the x direction and expand in the y direction. (d) The distorted bcc phase finally transforms back to the hcp phase but with a different configuration with axis along $[\bar{1}\bar{1}20]$ orientation. Dotted lines indicate the hcp-bcc interfacial boundaries. The initially transformed bcc phase is also preserved; it connects the initial $\langle\bar{1}100\rangle$-oriented and $\langle\bar{1}\bar{1}20\rangle$-oriented hcp phases.

Aside from the energetic aspects, the transformation path itself is quite different because unlike the Bain path or the Burgers path in usual MT, the transformation path here is not a straight line in the six-dimensional strain space but contains a turn in strain space. The initial $\langle\bar{1}100\rangle$-oriented and transformed $\langle\bar{1}\bar{1}20\rangle$-oriented NWs are connected via an intermediate, distorted bcc phase, similar to the role of a stacking fault in the splitting of a full dislocation. Although the

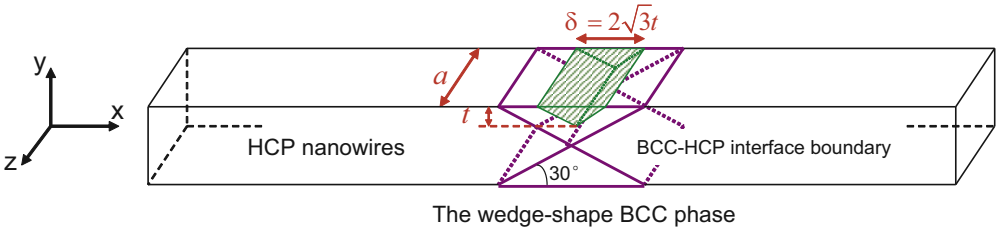

FIG. 3. (Color online) (a) Model for the inverse MTs in Zr nanowires. The bcc phase first nucleates at the top surface in y planes of the original hcp nanowire and then grows toward the ends and interior of the wire to form the two opposite wedge-shaped areas with 30° phase boundaries along the x axis. The dimensions of each wedge-shaped bcc nucleus is $2\sqrt{3}t$, t and a in x, y, and z directions, respectively (shown in green region). For the present Zr nanowire (21.2 nm × 2.1 nm × 2.1 nm) at 300 K, the two wedge-shaped bcc domains can penetrate the nanowire in y direction (shown in purple region), driven partially by elastic interactions.

bcc domains initially merge into one, shown in Fig. 2(c), it subsequently splits into four triangle-shaped bcc domains in Fig. 2(d). Two triangle-shaped bcc domains on one side then form a soliton like "transformation front" that translates along the nanowire (speed ~200 m/s) and converts the $\langle\bar{1}100\rangle$ wire to the new $\langle\bar{1}\bar{1}20\rangle$ orientation. The unique geometry of this transformation front (two bcc wedges) can be attributed to the quasi-one-dimensional nature of the nanowire and elasticity interaction associated with it, which cannot be seen in three-dimensional martensitic transformations. Conceptually, the two transformation fronts on left and right are analogous to a dislocation dipole of plus and minus full dislocations (each with some core splitting), except the soliton translation accomplishes lattice rotation of the hcp phase rather than lattice slip [Fig. 2(d)]

The two-step IMT-MT processes shown above are driven by the reduction in surface energy. For the present $\langle\bar{1}100\rangle$-oriented hcp nanowire (21.1 nm × 2.1 nm × 2.1 nm), the surface energy of the initial $\langle\bar{1}100\rangle$-oriented wire is 0.379 eV/atom, which is higher than that of transformed bcc (0.347 eV/atom) and that of $\langle\bar{1}\bar{1}20\rangle$-oriented hcp configuration (0.295 eV/atom). The reduction of surface energy drives the phase change from the initial $\langle\bar{1}100\rangle$-oriented hcp wire to the bcc and then the $\langle\bar{1}\bar{1}20\rangle$-oriented hcp wire. Once the initial $\langle\bar{1}100\rangle$ wire is converted to the $\langle\bar{1}\bar{1}20\rangle$ wire, the system becomes stable and cannot revert back to the initial $\langle\bar{1}100\rangle$ orientation.

The hcp-bcc IMT also follows the Burgers orientation relationship (OR),[5] $\{0001\}_{hcp}\|\{011\}_{bcc}$ and $\langle 11\bar{2}0\rangle_{hcp}\|\langle 1\bar{1}1\rangle_{bcc}$, as is the case for the normal bcc-hcp MT that combines shear and shuffle operations.[5,18] Specifically, two equivalent shear operations along the $[\bar{2}110]$ and $[1\bar{2}10]$ change the 120° angle in the hcp phase to the 109.47° angle in the bcc phase. Atoms also shuffle along the hcp $[1\bar{1}00]$ direction with displacement $\sqrt{3}a_0/6$ (a_0 is the lattice constant) to arrive at the bcc structure.

Our present observation of IMT is analogous to the asymmetry between solidification and melting of simple metals, where the liquid-to-crystal transformation requires finite undercooling, $\Delta T \equiv T_M - T > 0$, to overcome the nucleation barrier. However, the reverse crystal-to-liquid transition requires no superheating ($\Delta T = 0$) and can occur immediately when the bulk melting point (T_M) is reached, as long as a surface is present and

$$\gamma_S > \gamma_L + \gamma_{LS}, \tag{1}$$

where γ_S is the solid surface energy, γ_L is the liquid surface energy, and γ_{LS} is the liquid-solid interfacial energy. Equation (1) basically means the solid surface can be completely wet by its own liquid. If Eq. (1) is satisfied, there will be a thin disordered layer on the crystal surface (surface premelting), even for $T < T_M$. For our hcp-to-bcc case, a condition similar to Eq. (1) controls the IMT, i.e.,

$$\gamma_y^{hcp} > \gamma_y^{bcc} + 2\gamma^{bcc\text{-}hcp}/\sqrt{3}, \tag{2}$$

where γ_y^{hcp}, γ_y^{bcc}, and $\gamma^{bcc\text{-}hcp}$ is the relaxed surface energy for the hcp $\{\bar{1}\bar{1}20\}$ planes, the bcc surface (y plane in Zr NWs) energy and the bcc-hcp interface energy, respectively. We note that at the beginning of transformation the volume change and total elastic energy are negligible in the immediate proximity of free surfaces. We therefore calculate γ_y^{hcp} and γ_y^{bcc} by constructing a slab with y plane as the exposed surface and periodic boundary condition along the other two directions and performing a global minimization using a conjugate gradient (CG) algorithm at 0 K, and we obtain the values of γ_y^{hcp} and γ_y^{bcc} from the energy per area in excess of that of the slab without free surfaces. Similarly, the $\gamma^{bcc\text{-}hcp}$ is calculated by constructing an hcp-bcc interface based on the Burgers OR (Ref. 5) and minimizing the system energy along the direction that is normal to the interface using the same CG algorithm. The calculated values of γ_y^{hcp}, γ_y^{bcc}, and $\gamma^{bcc\text{-}hcp}$ at 0 K are 9.62, 9.17, and 0.10 eV/nm^2 respectively, which proves the validity of Eq. (2).

Unlike surface melting, in which the interface between liquid and solid is incoherent, the IMT-formed bcc and the original hcp form a coherent phase boundary. The bcc phase first occurs on the $\{11\bar{2}0\}$ surface planes, and propagates toward the ends and the interior of the NW, and then forms two opposite wedge-shaped areas with an interface boundary by rotating 30° along axis direction (schematically shown in Fig. 3). Therefore, the Helmholtz free energy difference ΔF between the hcp NW with bcc structure in $\{11\bar{2}0\}$ planes, and an entirely hcp NW, can be given by

$$\Delta F = \frac{1}{2}\delta a t \Delta F_{volume}^{bcc\text{-}hcp} + 4at\gamma^{bcc\text{-}hcp} + \delta t(\gamma_z^{bcc} - \gamma_z^{hcp}) + \delta a(\gamma_y^{bcc} - \gamma_y^{hcp}), \tag{3}$$

where $\delta(=2\sqrt{3}t)$, t is the thickness and a the side length of

the wedge-shaped nucleus (see Fig. 3), respectively. In addition, $\Delta F_{\text{volume}}^{\text{bcc-hcp}}$ (2.22 eV/nm^3 or 0.052 eV/atom at 0 K) refers to the ΔF of bulk bcc and hcp crystals, which is actually the potential energy difference between bcc and hcp crystals at 0 K. γ_z^{hcp} and γ_z^{bcc} refer to the relaxed surface energies of $\{0001\}$ hcp and $\{011\}$ bcc in z planes, which are 8.00 eV/nm^2 and 8.14 eV/nm^2 at 0 K, respectively (calculated by the same method as for γ_y^{hcp} and γ_y^{bcc}). From Eq. (3), we see that ΔF is closely related to the dimensions (t and a) of the bcc nuclei. For a fixed a value, ΔF should be a function of t. Before the occurrence of bcc, $t=0$, $\Delta F=0$. With increase in t, ΔF decreases which indicates that the IMT occur spontaneously. However, the obstacle terms [the first three terms of Eq. (3)] increase quickly with the growth of bcc nuclei and will gradually overpower the driving terms [the last term of Eq. (3)]. That is, there is a critical thickness t^* at which $d(\Delta F)/dt=0$. By the time t reaches t^*, the bcc phase has no more incentive to grow, since ΔF will start to rise. The IMT is thus self-limiting, stopping once the size of the bcc phase reaches a critical length scale. For $a=2.1$ nm, $t^*=0.07a$ at 0 K but increases with increasing temperature as $\Delta F_{\text{volume}}^{\text{bcc-hcp}}$ becomes smaller.

We have also verified that IMT in Zr nanowire is caused by the absolute surface energy difference, not the compressive stresses inside the nanowire due to surface stress. That is to say, were there no surfaces, but only infinite bulk hcp and bcc crystals, there can be no hcp→bcc transformation even if a constant external stress (of equal magnitude as that due to surface stress in the nanowire) is applied.

Fcc or bcc NWs are known to undergo lattice reorientation via twinning (motion of twin boundaries)[8–11] to minimize their surface energy. It is therefore important to address the question why the Zr NW prefers the two-step IMT-MT route, i.e., IMT from $\langle\bar{1}100\rangle$ hcp to bcc and normal MT from bcc to $\langle\bar{1}\bar{1}20\rangle$ hcp, rather than the direct twinning between $\langle\bar{1}100\rangle$-oriented and $\langle\bar{1}\bar{1}20\rangle$-oriented configurations. To this end, we calculate and compare the energy barrier at 0 K for each path. As shown in Fig. 2, the two-step MT path has three stages: the IMT, bcc distortion and bcc-to-hcp MT. As the forward normal MT is known to occur easily for Zr at RT, its energy barrier is presumably very low. As for the IMT, the hcp-bcc transformation is just the opposite of the normal bcc-hcp MT that combines shear and shuffle operations. The energy landscape is mapped out in Fig. 4(a) to find the energy barrier for IMT, as a function of shear and shuffle parameters. We find that the IMT easily occurs along the diagonal where the minimum energy barrier is 0.052 eV/atom. As far as the bcc distortion is concerned, the [011]-axis configuration undergoes distortion to [100]-axis configuration with shrinkage along x-$[10\bar{1}]$, expansion along y-[010] and almost no change in z-[101], and the volume remains almost constant during the process. We can then obtain the potential energy as a function of lattice parameter ratio from $\sqrt{2}/2$ ([011] configuration) to $\sqrt{2}$ ([100] configuration), similar to the Bain transformation.[19] As shown in Fig. 4(b), the energy barrier for such bcc distortion is 0.021 eV/atom. It is noted that, the energy landscape for IMT and bcc distortion are calculated at 0 K with periodic boundary conditions, and there is no relaxation during the movement of atoms.

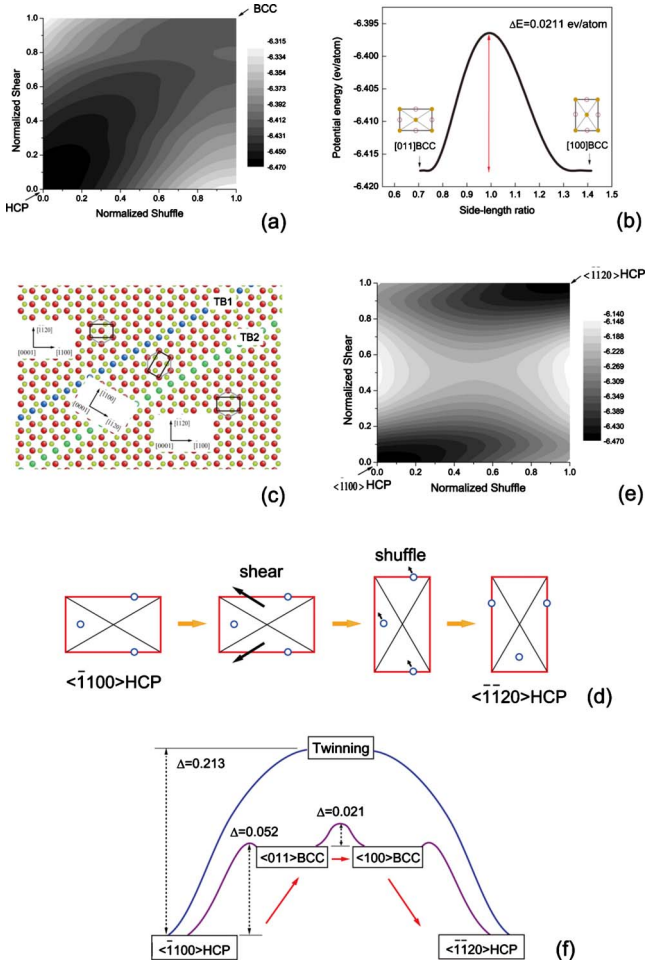

FIG. 4. (Color online) (a) Bulk potential energy map for hcp→bcc phase transition. The energy barrier along the optimum path is 0.052 eV/atom. (b) Bulk potential energy surface for bcc distortion as a function of lattice parameter ratio from $\sqrt{2}/2$ in [011]-axis configuration to $\sqrt{2}$ in [100]-axis configuration. The energy barrier is 0.021 eV/atom. (c) Atomic configurations for two types of twin boundaries between the initial and reoriented hcp crystals. These are referred to TB1 with a high energy and TB2 with a low energy, respectively. (d) Schematic illustration of direct twinning deformation from $\langle\bar{1}100\rangle$-oriented hcp to $\langle\bar{1}\bar{1}20\rangle$-oriented hcp with the combination of shear and shuffle operations. (e) Bulk potential energy map for deformation twinning from $\langle\bar{1}100\rangle$-oriented hcp to $\langle\bar{1}\bar{1}20\rangle$-oriented hcp. The energy barrier along the optimum path is 0.213 eV/atom. (f) Schematic illustration of the reorientation by the two-step phase transition (hcp→bcc IMTs, then bcc→hcp MT) versus one-step hcp→hcp transition by deformation twinning. The unit for energy barrier Δ is eV/atom.

We calculate next the energy barrier by direct twinning from $[\bar{1}100]$ hcp to $[\bar{1}\bar{1}20]$ hcp. The two configurations can form a $\langle\bar{2}110\rangle/\{\bar{1}100\}$-type twin system with two types of twin boundaries [TB1 and TB2 as shown in Fig. 4(c)]. Unlike fcc and bcc metals, both shear and shuffle are needed to for twinning in hcp. The shear (along $[\bar{2}110]$ and $[\bar{1}2\bar{1}0]$ directions) changes the angle from the 60° in $\langle\bar{1}100\rangle$ hcp to the 120° in $\langle\bar{1}\bar{1}20\rangle$ hcp, and the atomic shuffle moves atoms

by $a_0/3$ along the $[\bar{2}110]$ direction [as illustrated in Fig. 4(d)]. Similar to the calculation for the IMT path, an energy contour map for this path at 0 K is plotted in Fig. 4(e), giving the minimum energy barrier as 0.213 eV/atom. The comparison schematically shown in Fig. 4(f) clearly indicates that the two-step MT is a much more energetically favorable path than direct twinning.

IV. CONCLUSION

In summary, in hcp Zr NWs the surface-energy reduction drives a hcp→bcc IMT, in contrast to the usual bcc→hcp MT that is driven by the volume bulk energy. Our MD simulations show that the initially $\langle\bar{1}100\rangle$-oriented hcp NW first undergoes IMTs into surface-bound bcc domains, and the metastable bcc domains subsequently meet, react and undergo normal MT to another $\langle\bar{1}\bar{1}20\rangle$-oriented hcp configuration, resulting in the reorientation of the NW. Because the characteristic size scale of the system, i.e., diameter of the NW, is comparable to the self-limiting length scale r^* of IMT, the IMT can penetrate the wire, triggering the next stage of normal MT. In much thicker surface-bound slabs where $H \gg r^*$, we expect IMT to be self-limiting (at least in the thickness direction), which is fundamentally different from normal MTs in the bulk.

ACKNOWLEDGMENTS

This work was supported by NSFC (Grants No. 50771079, No. 50720145101, and No. 50831004) and the 973 Program of China (Grant No. 2010CB631003) as well as 111 project (B06025). J.L. acknowledges support by NSF under Grant No. CMMI-0728069, MRSEC under Grant No. DMR-0520020, ONR under Grant No. N00014-05-1-0504, and AFOSR under Grant No. FA9550-08-1-0325. X.D. and T.L. also acknowledge support from the U.S. DOE at LANL (Grant No. DE-AC52-06NA25396). E.M. was supported in part by US-DOE, Basic Energy Sciences, Division of Materials Science and Engineering (No. DE-FG02-09ER46056).

*Corresponding author.
†dingxd@mail.xjtu.edu.cn
‡liju@seas.upenn.edu
§ema@jhu.edu

[1] J. W. Christian, G. B. Olson, and M. Cohen, J. Phys. IV **05**, C8-3 (1995).
[2] K. Otsuka and X. Ren, Prog. Mater. Sci. **50**, 511 (2005).
[3] C. Zener, *Elasticity and Anelasticity of Metals* (University of Chicago Press, Chicago, 1948).
[4] X. Ding, T. Suzuki, X. Ren, J. Sun, and K. Otsuka, Phys. Rev. B **74**, 104111 (2006).
[5] W. G. Burgers, Physica (Amsterdam) **1**, 561 (1934).
[6] G. B. Olson and M. Cohen, in *Proceedings of an International Conference on Solid-Solid Phase Transformations* (TMS, Warrendale, PA, 1981), p. 1145.
[7] D. A. Porter and K. E. Easterling, *Phase Transformations in Metals and Alloys* (Chapman and Hall, London, 1992).
[8] J. Diao, K. Gall, and M. L. Dunn, Phys. Rev. B **70**, 075413 (2004).
[9] W. W. Liang, M. Zhou, and F. J. Ke, Nano Lett. **5**, 2039 (2005).
[10] H. S. Park, K. Gall, and J. A. Zimmerman, Phys. Rev. Lett. **95**, 255504 (2005).
[11] S. Li, X. Ding, J. Li, X. Ren, J. Sun, and E. Ma, Nano Lett. **10**, 1774 (2010).
[12] M. Igarashi, M. Khantha, and V. Vitek, Philos. Mag. B **63**, 603 (1991).
[13] M. I. Mendelev and G. J. Ackland, Philos. Mag. Lett. **87**, 349 (2007).
[14] S. Nosé, J. Chem. Phys. **81**, 511 (1984).
[15] W. G. Hoover, Phys. Rev. A **31**, 1695 (1985).
[16] S. Plimpton, J. Comput. Phys. **117**, 1 (1995).
[17] J. Li, Modell. Simul. Mater. Sci. Eng. **11**, 173 (2003).
[18] M. Sanati, A. Saxena, T. Lookman, and R. C. Albers, Phys. Rev. B **63**, 224114 (2001).
[19] E. C. Bain and N. Y. Dunkirk, Trans. AIME **70**, 25 (1924).